Nanoscale

PAPER

View Article Online
View Journal | View Issue

Check for updates

Cite this: *Nanoscale*, 2025, **17**, 27637

Enhanced magnetic and optical properties of $Y_3Fe_5O_{12}$ (YIG) films with Au nanoinclusions

Lizabeth Quigley,[a] Katrina Evancho,[a] Claire A. Mihalko,[a] Yizhi Zhang,[a] Chang Liu,[a] Max Chhabra,[a] Bharat Giri,[b] Jialong Huang,[a] Abhijeet Choudhury,[a] Jeremy Gan,[a] Zhengliang Lin,[c] Xiaoshan Xu,[b,d] Ping Lu,[e] Raktim Sarma,[e,f] Aleem Siddiqui[e] and Haiyan Wang *[a,c]

Received 15th September 2025,
Accepted 30th October 2025

DOI: 10.1039/d5nr03907j

rsc.li/nanoscale

$Y_3Fe_5O_{12}$ (YIG) thin films are well known for their ferrimagnetic insulating property and low Gilbert damping coefficient (α), allowing them to be used for various spintronic applications and as magneto-optical isolators for photonic devices. Instead of doping, incorporation of plasmonic metals as nanoinclusions could be a promising route for improved magneto-optical coupling properties. In this work, YIG–Au nanocomposites have been deposited with ferrimagnetic insulating YIG as the matrix and Au nanoinclusions which introduce plasmonic absorption, optical anisotropy, and hyperbolic properties. Films with varying Au nanoinclusion densities have been processed and annealed to compare with the as-deposited ones. The films that had low Au nanoinclusion density and were annealed presented a lower magnetic damping coefficient of 2.84×10^{-4} than the pure YIG film (9.66×10^{-4}). The as-deposited film with the highest Au density shows the strongest hyperbolic properties among all samples. These results demonstrate that both magnetic damping and optical properties can be tuned through deposition conditions in YIG–Au nanocomposite thin films, allowing for a balance of both properties. This YIG–Au nanocomposite system presents promising potential in next-generation opto-spintronic devices.

Introduction

Materials for spintronic devices have been of interest in the scientific community for many years, driven by the need for improved computational performance.[1–3] One material of great interest is yttrium iron garnet ($Y_3Fe_5O_{12}$, YIG), since its first demonstration in 1957.[3] YIG is well-suited for spintronic applications because of its ferrimagnetic nature, electrical insulation, and a low Gilbert damping coefficient (α), which can range from 2×10^{-5} to 8.9×10^{-3} depending on the deposition conditions, with the lowest and best values ranging from 2×10^{-5} to 5×10^{-5}.[4–7] These properties make YIG attractive for use in devices such as spin-wave guides, memory devices, or spin logic devices.[2] YIG is also prized for its high optical transparency, allowing it to be used for magneto-optical devices such as Faraday rotators, optical isolators, and quantum information processing.[8] This optical transparency, while beneficial in these applications, limits YIG's use in systems where coupling between light and spin dynamics could enable more advanced functionalities. Developing this capability could allow for novel opto-spintronic devices where light could control or manipulate spin waves.[9,10] However, deposition of high-quality YIG can be challenging due its complex garnet crystal structure and large lattice parameter. Gadolinium gallium garnet ($Gd_3Ga_5O_{12}$, GGG) is one of the most common substrates used for YIG growth due to the close lattice parameters (a_{GGG} = 12.383 Å *vs.* a_{YIG} = 12.376 Å) and other substrates such as quartz, silicon, or yttrium aluminum garnet (YAG) have also been explored.[3,11–13] Pulsed laser deposition (PLD) is one of the most widely used deposition techniques for YIG thin films due to its high-energy growth and ability to maintain the target stoichiometry on the thin film, both of which are desirable for complex thin films.[14] While other techniques such as sol–gel and magnetron sputtering can also deposit YIG films, PLD remains the preferred approach.[3] Other deposition parameters also need to be carefully controlled. For example, low oxygen partial pressure during deposition leads to vacancy formation within the YIG film, degrading film quality and properties.[15] Post-deposition

---

[a] *School of Materials Engineering, Purdue University, West Lafayette, Indiana 47907, USA. E-mail: hwang00@purdue.edu*

[b] *Department of Physics and Astronomy, University of Nebraska-Lincoln, Lincoln, Nebraska 68588, USA*

[c] *School of Electrical and Computer Engineering, Purdue University, West Lafayette, Indiana 47907, USA*

[d] *Nebraska Center of Materials and Nanoscience, University of Nebraska-Lincoln, Lincoln, Nebraska 68588, USA*

[e] *Sandia National Laboratories, Albuquerque, New Mexico 87185, USA*

[f] *Center for Integrated Nanotechnologies, Sandia National Laboratories, Albuquerque, New Mexico 87175, USA*

annealing, especially under an oxygen atmosphere, is vital for stabilizing the garnet crystal structure, minimizing oxygen deficiencies, and reducing the Gilbert damping coefficient.[16]

Much work has been focused on doping YIG with other elements for enhanced ferromagnetic and magneto-optical coupling. For example, cerium-doping (Ce:YIG) has been incorporated in the Y sublattices for enhancing the magneto-optical response.[17–19] Bismuth-doping (Bi-YIG) has been introduced for strain tuning of the magnetic anisotropy in YIG films.[20–22] On the other hand, incorporating a YIG-based nanocomposite design could allow for novel hybrid metamaterials, *i.e.*, artificially engineered materials with two or more phases that do not exist in nature.[23] Different from the doping methods, the secondary phases incorporated into the YIG-based hybrid metamaterials could allow for additional functionalities to be integrated in the systems without varying the lattice structure and intrinsic properties of YIG significantly. For example, some of the multilayer Au–YIG, Ag–YIG, and Cu–YIG structures have been processed previously with the goal to study magneto-optical coupling and spin–orbit coupling between the magnetic and non-magnetic layers.[24–28]

Beyond the typical multilayers and particle-in-matrix nanocomposites as hybrid metamaterials, a new class of nanocomposites has recently evolved in various systems, namely oxide–metal based vertically aligned nanocomposites (VANs). Au, Ag, Co, Cu, Ni, and Fe have been incorporated into various dielectric oxides as oxide–metal hybrid metamaterials, such as CeO_2–Au, ZnO–Au, $LiNbO_3$–Au, $BaZrO_3$–Co, ZnO–Cu, ZnO–Ni, VO_2–Ni, $BaTiO_3$–Fe, and CeO_2–NiFe.[23,29–42] Many of these VAN hybrid metamaterials show enhanced optical anisotropy and even hyperbolic properties.[23,29–31,36] Several of these are ferromagnetic with enhanced out-of-plane magnetic anisotropy and/or magneto-optical coupling properties.[32–35,37–42]

In this work, we propose to explore the effects of Au incorporation into the YIG matrix on the epitaxial growth quality, the overall ferrimagnetic and optical properties, their ferromagnetic resonance (FMR) properties, and their potential for YIG-based hybrid metamaterials with multifunctionalities and property tunability. Such systems can be grown in a one-step deposition PLD process as illustrated in Fig. 1. This approach is advantageous as PLD is already established for high quality YIG film growth.[3] In YIG–Au VANs, the inclusion of Au is expected to reduce the overall optical transparency due to increased absorption. In addition, the Au nanoinclusions could also introduce a localized surface plasmon resonance (LSPR), a characteristic of Au and other noble metals, where the overall composite's optical and magneto-optical responses can be tuned by specific incident wavelengths and tailoring

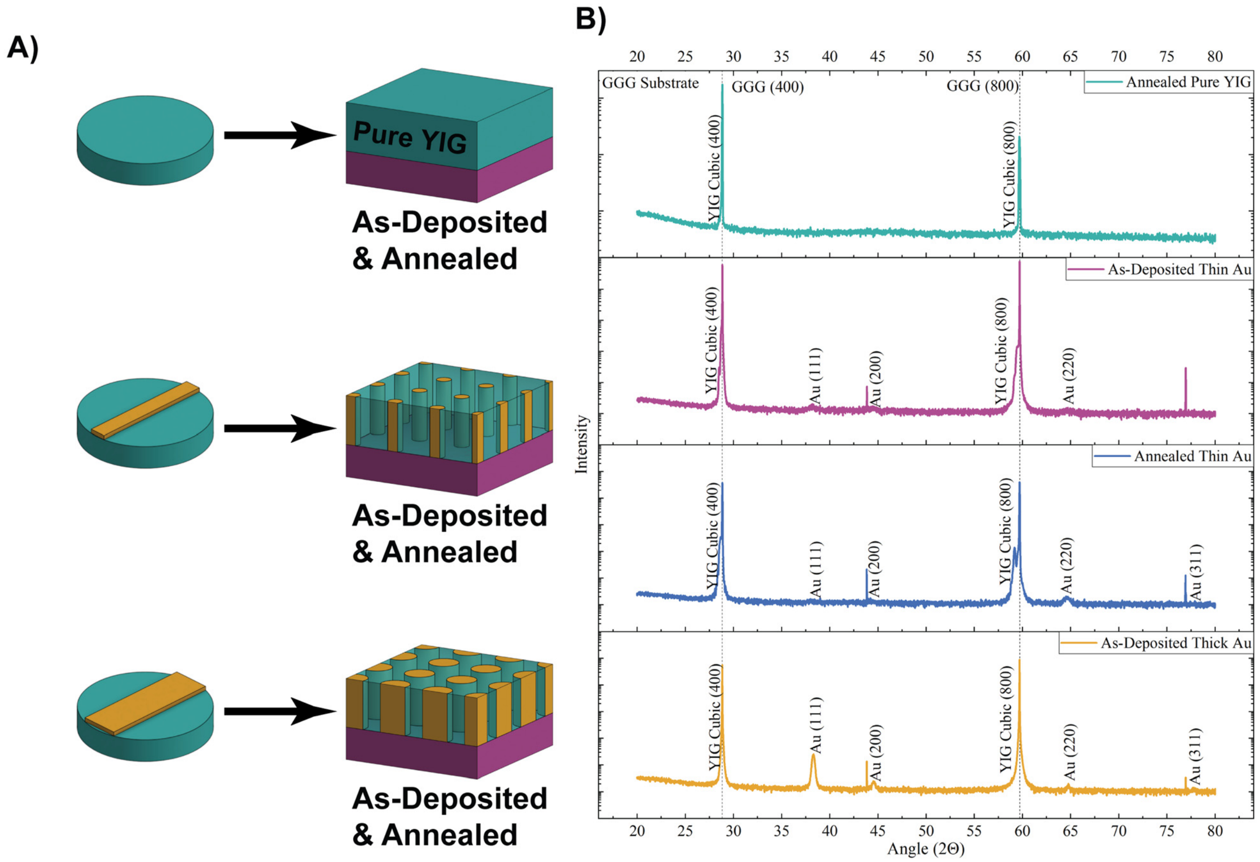

Fig. 1 (A) Ideal schematic drawing of the six films deposited using the three targets. (B) XRD θ–2θ of the Annealed Pure YIG, As-Deposited with Thin Au Strip, Annealed with Thin Au Strip, and As-Deposited with Thick Au Strip thin film samples.

the Au morphologies.[43] We anticipate enhanced optical absorption, with tuning of magnetic anisotropy, and FMR properties, a measurement used to evaluate the magnetic damping properties. The proposed YIG-based hybrid VAN structures could find unique applications in future integrated photonic structures with tailorable optical responses and desired magnetic properties by combining LSPR effects with the magnetic properties of YIG. This could allow light to actively modulate the spin transport, a key requirement for future opto-spintronic devices.

Methods

In this work, a total of six YIG films on GGG substrates (100) were deposited, as demonstrated in Fig. 1A. Three target configurations were used: a pure YIG target, the same pure YIG target with a Thin Au Strip with a width of 2.6 mm pasted on it; and the same pure YIG target with a Thick Au Strip with a width of 5.7 mm pasted on it. Fig. 1A shows the schematics of the three targets, and Thin and Thick refer to the width of the Au strips used during deposition. Four of the films deposited on the GGG substrates are the focus of this work: Annealed Pure YIG, As-Deposited with Thin Au Strip, Annealed with Thin Au Strip, and As-Deposited with Thick Au Strip. The results of the remaining films can be found in the SI Fig. S2–S12. The same depositions were also performed on $SrTiO_3$ (STO) (100) substrates, with all results shown in SI Fig. S13–S21, primarily to allow for transmission electron microscopy (TEM) imaging of all films to be performed. Additionally, four more samples were also deposited, two on GGG and two on STO, with a YIG–Au buffer layer below a YIG single layer; these samples' data can be found in the SI. Each substrate pair included an as-deposited sample and an annealed counterpart, as shown in Fig. 1A. These results for every sample can be found in the SI with the other data of the same substrate. SI Fig. S2–S12 show the details of all samples deposited on GGG substrates, and SI Fig. S13–S21 show the details of samples deposited on STO substrates. Full deposition parameters can be found in the Experimental methods section, and a table summarizing all sample configurations can be found in the SI as Table S1. To characterize the structural, optical, and magnetic properties of these films, X-ray diffraction (XRD), ellipsometry, transmittance measurement, ferromagnetic resonance (FMR), transmission electron microscopy (TEM), scanning transmission electron microscopy (STEM), and energy dispersive X-ray spectroscopy (EDS) were performed and can be found in the main body of the paper. The magnetic hysteresis loops of each film were also measured and can be found in SI Fig. S7 and S18.

Results and discussion

X-ray diffraction (XRD) was performed on all deposited films to confirm the YIG phase and determine if Au was deposited as expected on the nanocomposite films. As shown in Fig. 1B, all four films had the YIG cubic phase which usually demonstrates the best magnetic properties including the lowest Gilbert damping coefficient among all the possible YIG phases. It is worth noting that YIG and GGG have lattice parameters that are very close to each other, with the lattice parameters of YIG and GGG being 12.376 Å and 12.383 Å, respectively. This results in the cubic YIG peak appearing as a shoulder peak with the GGG peak. The extra sharp peaks appearing in the bottom three samples are other GGG substrate peaks. It is vital for the YIG phase to grow as defect-free to minimize negative effects on the magnetic damping like two-magnon scattering. The addition of Au, while allowing for new optical properties, could result in reduced magnetic properties because it is an introduced defect. All the films with Au incorporated during growth show Au peaks in the XRD results. On comparing the relative intensities with that of the GGG substrate peak, the As-Deposited with Thick Au Strip sample shows the strongest Au peaks, supporting that this sample has the highest Au composition as expected from the thicker Au strip used during the deposition. Of the two Thin Au Strip samples, the As-Deposited sample has more consistent Au peak intensities while the Annealed sample has a higher intensity Au (220) peak. This shows that annealing could affect the morphology or the texture of Au nanoinclusions in the films and thus result in the differences in XRD peak intensities. The effect of the Au nanoinclusions can also be seen in the YIG growth by observing the Thin Au Strip samples. The more apparent YIG cubic peaks for these samples would suggest that the Au phase allowed for better growth of the YIG phase, allowing for a stronger response to be seen during this measurement. This can also be seen through the Au Buffer samples, which show the most pronounced YIG cubic peaks, as seen in SI Fig. S2 and S3. The introduction of the YIG–Au buffer layer could facilitate the nucleation of the following YIG layer. Prior work such as that on lithium niobate ($LiNbO_3$, LNO) grown using a LNO–Au seed layer has demonstrated the benefit of the LNO–Au seed layer for promoting the nucleation and the single domain growth of LNO.[44] For the YIG–Au system in this work, continuing the co-deposition of YIG–Au for the entire film allowed for better results, with the strain generated along the interfaces helping to promote the formation of more crystalline cubic YIG phases. The Au Buffer samples have their YIG cubic peak slightly offset from the GGG substrate peak, likely due to a higher stress in these films, showing how the continuation of the Au phase is necessary for a reduction in stress. The importance of annealing is still shown as the Annealed Thin Au strip sample has a sharper YIG (800) peak compared to that of the As-Deposited Thin Au strip sample.

To analyze the microstructure, TEM, STEM, and EDS were performed on the films as seen in Fig. 2. Most of these images are of the YIG samples grown on STO as these were able to be prepared by hand instead of using a focused ion beam (FIB) cut as needed for the samples grown on GGG. Fig. 2A1–A4 show the Annealed Pure YIG sample grown on STO. As seen in SI Fig. S13 and S14, the STO samples grew orthorhombic YIG

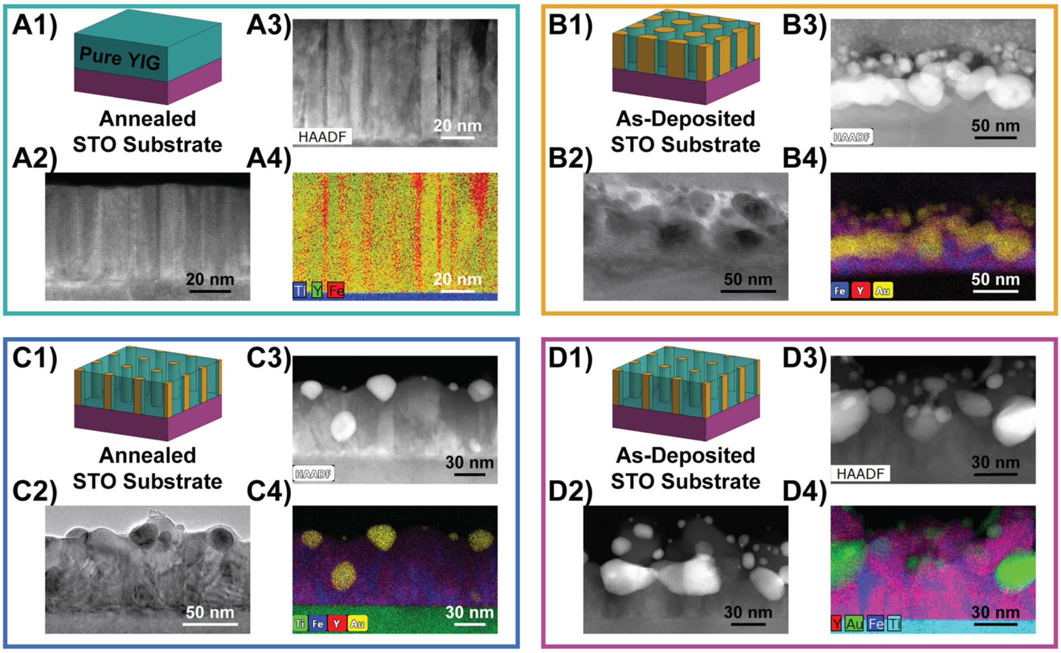

Fig. 2 (A) The Annealed Pure YIG sample on STO, (B) As-Deposited with Thick Au Strip sample on STO, (C) Annealed with Thin Au Strip sample on STO, and (D) As-Deposited with Thin Au Strip sample on STO. (1) Ideal schematic drawing of the sample, (2) TEM image of the sample (3) STEM image for the corresponding EDS map of the sample, and (4) EDS map of the sample.

instead of cubic YIG. This is due to the difference in STO's lattice parameters when compared to those of YIG (a_{STO} = 3.905 Å *vs.* $a_{\text{YIG, cubic}}$ = 12.376 Å, $a_{\text{YIG, orthorhombic}}$ = 5.27 Å, $c_{\text{YIG, orthorhombic}}$ = 7.59 Å) putting higher strain on the film. Fig. 2A4 shows that the samples grown on STO have phase separation with yttrium-rich and iron-rich areas. Yttrium oxide and iron oxide do not show up on the sample's XRD measurement, so these are richer areas of YIG. Due to the orthorhombic lattice parameter still being larger than that of STO, the separation of the Y-rich and Fe-rich areas could have allowed for further strain relaxation of these films during the growth. The regular variation between Y-rich YIG and Fe-rich YIG seen in Fig. 2A3 and A4 supports this. This trend continues with the other samples grown on STO and helps explain some of the properties seen for these samples in SI Fig. S15–S20, which will not be discussed in detail here.

Fig. 2B1–B4 show the As-Deposited with Thick Au Strip sample on STO. It can be clearly seen that out of the four samples grown on STO, this has the highest Au nanoparticle density, as expected. Looking at the other two films deposited on STO, it is possible to see that in all the films, the Au nanoparticle cluster moves towards the top of the film rather than being evenly distributed throughout the entire film thickness. This shows that in this system, there is a lower surface energy for the Au nanoparticles to grow on the orthorhombic YIG instead of the STO substrate. The Annealed with Thin Au Strip sample on STO shown in Fig. 2C1–C4 has less Au than the As-Deposited with Thick Au Strip sample on STO, and the smallest, but most consistent, average nanoparticle size of the samples grown on STO. A few smaller Au nanoparticles, like the ones seen in the next sample, are still present, but longer annealing time would allow the thermal energies to help these fully coalesce with the other nanoparticles. The comparison of the As-Deposited with Thin Au Strip sample on STO is shown in Fig. 2D1–D4. This sample has larger nanoparticles again, as seen in the As-Deposited with Thick Au Strip sample, but the lower Au content in this deposition results in reduced Au volume fraction. The lack of annealing allows for Au nanoparticles of varying sizes, with both larger and smaller size than average nanoparticles existing in this sample. Altogether, for the YIG–Au system, annealing has a large effect on the size and distribution of the Au nanoparticles within the film. The thicknesses of each film were also analyzed, with the four films shown here having thicknesses of 51.0 nm for Annealed Pure YIG, 76.9 nm for As-Deposited with Thin Au Strip, 74.8 nm for Annealed with Thin Au strip, and 83.9 nm for the As-Deposited with Thick Au Strip. SI Table S7 includes the thicknesses of all of the films deposited on STO substrates. On average, the as-deposited films have a larger film thickness than the annealed films, providing another insight into how annealing affects these films.

Two of the samples grown on GGG are also shown, prepared with a FIB cut. Due to YIG's insulating nature, a Pt layer was deposited on top of the films to allow for these TEM samples to be made. Fig. 3A1–A4 show the Annealed Pure YIG sample on GGG. Unlike the samples grown on STO, the sample shows uniform Y and Fe distribution throughout the sample, suggesting that GGG is the more optimal substrate for growth. The As-Deposited with Thin Au Strip sample on GGG (Fig. 3B1–B4) shows that YIG–Au can grow in a VAN microstruc-

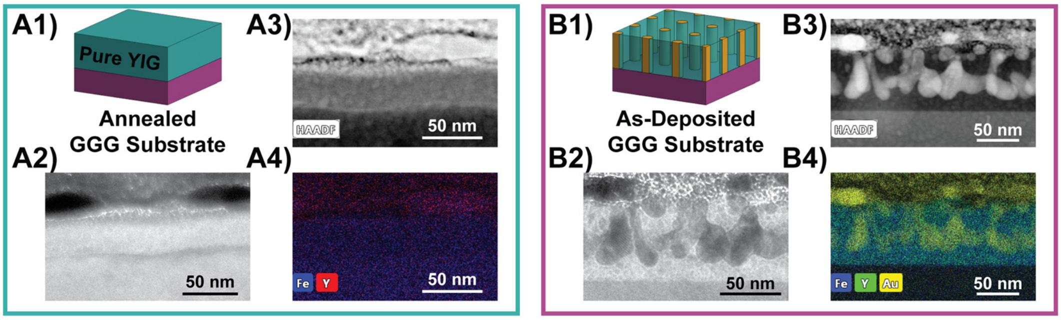

Fig. 3 (A) The Annealed Pure YIG sample on GGG and (B) As-Deposited Thin Au Strip sample on GGG. (1) Ideal schematic drawing of the sample, (2) TEM image of the sample, (3) STEM image for the corresponding EDS map of the sample, and (4) EDS map of the sample.

ture as this film grew the Au as nanopillars instead of nanoparticles. The Au nanopillars start to form only after a layer of YIG has been deposited, showing that for samples grown on the GGG substrates the lower surface energy of cubic YIG allows the Au phase to grow more easily compared to the higher surface energy of the substrate itself. This film also has a lower surface roughness than that on STO (Fig. 2D1–D4), likely due to the better matching substrate lattice allowing for more epitaxial growth and a lower surface energy during the deposition. The thickness of these films was also measured, with that of the Annealed Pure YIG sample being 38.3 nm and that of the As-Deposited with Thin Au Strip sample being 76.8 nm. SI Table S4 lists the thicknesses of all samples deposited on GGG with TEM imaging performed. This change in film thickness indicates that the Au phase supports YIG deposition compared to the Pure YIG film. Observing the microstructure allows for the tunability of the films to be demonstrated as the Au distribution varies between each set of samples.

To determine the effect of the addition of the Au nanoinclusions on the YIG films, optical spectroscopic ellipsometry and transmittance measurements were performed on all films, as shown in Fig. 4. SI Fig. S1 shows a closer view of the near zero region for the ellipsometry data. The Annealed Pure YIG and the As-Deposited with Thin Au Strip samples have their real and imaginary permittivity shown in Fig. 4A1 and A2. The Annealed Pure YIG sample shows no obvious optical anisotropy in the measured wavelength and shows minimal absorption evidenced by its flat curve at high wavelengths, indicating YIG's high optical transparency. The flatness of the real permittivity also demonstrates YIG's stable refractive index, which is characteristic of the dielectric nature of YIG.[3] The imaginary permittivity for the Annealed Pure YIG sample remains close to zero at all measured wavelengths, further suggesting its low loss characteristics. In Fig. 4A1, the As-Deposited with Thin Au Strip sample is the first to show optical anisotropy and hyperbolic properties, which could be attributed to the addition of the Au nanoinclusions. The anisotropy is indicated by the need to fit the data using two distinct directions: the parallel (‖) or in-plane direction, and the perpendicular (⊥) or out-of-plane direction. These new optical anisotropies are due to interactions between the polarized light and the anisotropic YIG–Au nanostructures, which can support localized surface plasmon resonances (LSPRs). This is when the electrons in the Au enhance light absorption and scattering depending on its structure and orientation to the light, leading to different responses in different directions. The better data fit using the anisotropic model, with reduced error, shows that the material has different optical properties in these two directions instead of an isotropic fit as seen in the Annealed Pure YIG sample. Hyperbolic properties are seen when the real part of the permittivity shows opposite signs in the two orientations. The As-Deposited with Thin Au Strip sample shows a Type-I hyperbolic behavior because the perpendicular (⊥) permittivity is negative, showing that the YIG matrix behaves more as a dielectric and the Au nanoinclusions show metallic behavior. The two hyperbolic regions observed in this film occur between 871–1390 nm and 1624–2000 nm, respectively. A possible reason for the two hyperbolic regions could be that the as-deposited Au nanoinclusions have multiple growth orientations and sizes allowing for different plasmonic resonances and light interactions at the different wavelength regions. From the imaginary permittivity of the As-Deposited with Thin Au Strip sample in Fig. 4A2, optical anisotropy can still be observed. It is worth noting that the parallel (‖) direction is still relatively flat at higher wavelengths, above 1000 nm, showing that the film retains much of its optical transparency, similar to that of pure YIG.

Fig. 4B1–B2 present the real and imaginary permittivity for the Annealed with Thin Au Strip sample and the As-Deposited with Thick Au Strip sample. Both films, because of the Au nanoinclusions, exhibit optical anisotropy and hyperbolic properties, but differ from the case of the As-Deposited with Thin Au Strip sample. The Annealed with Thin Au Strip sample still displays Type-I hyperbolic behavior, but with only one hyperbolic region at 712–873 nm, a narrower range compared to the multiple hyperbolic regions seen in the previous sample. By retaining the optical anisotropy, this sample demonstrates how the parallel (‖) and perpendicular (⊥) permittivity values represent the metallic-like and dielectric-like responses, respectively. Both behaviors are present in hyperbolic films, but with only one dominating depending on the measurement

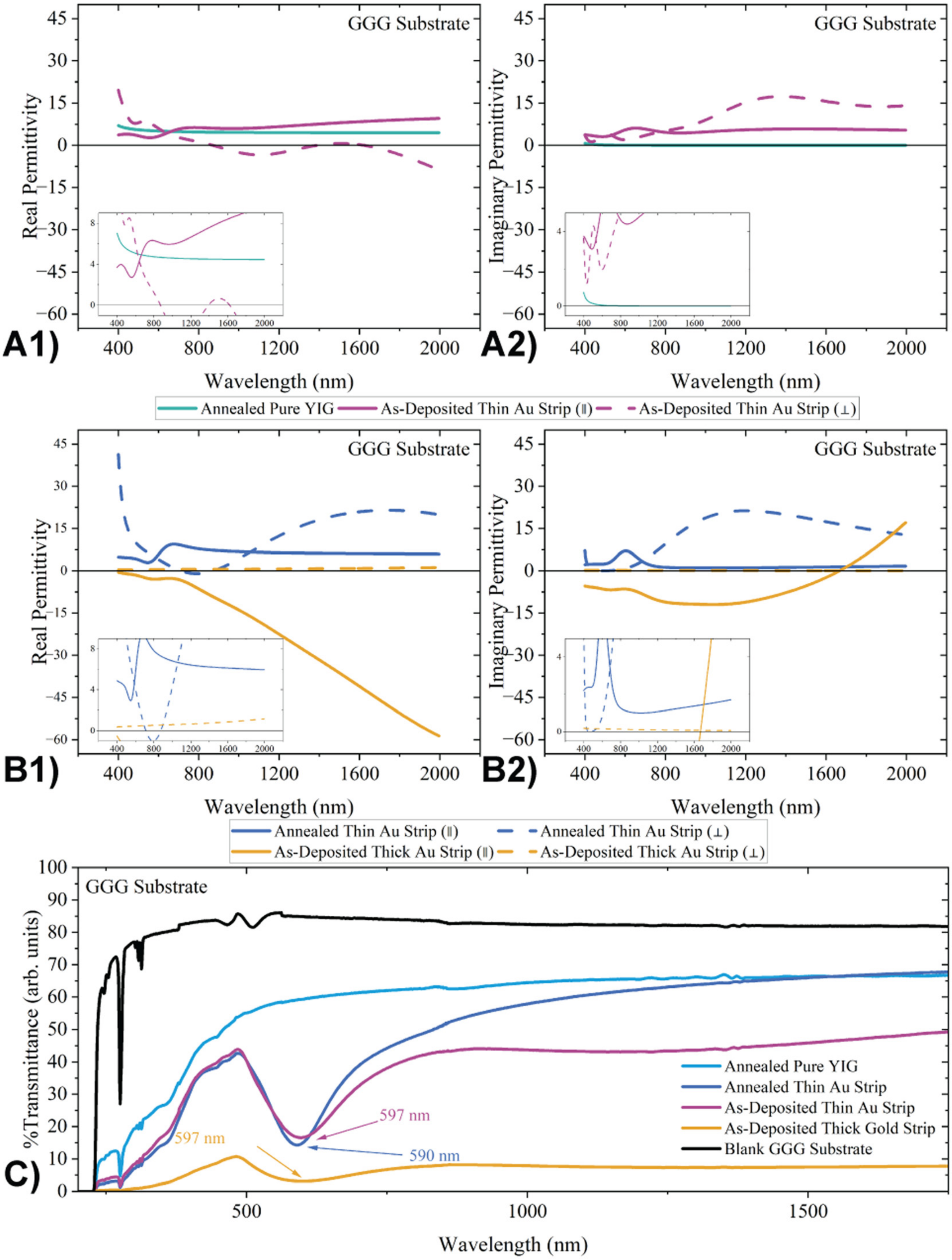

Fig. 4 (A1) Real permittivity and (A2) imaginary permittivity of the Annealed Pure YIG and As-Deposited with Thin Au Strip samples. (B1) Real permittivity and (B2) Imaginary permittivity of the Annealed with Thin Au Strip and As-Deposited with Thick Au Strip samples. (C) Transmittance data for all four samples with plasmonic resonances marked.

wavelength range. By annealing the Au nanoinclusions, the sample was able to tune this response. As discussed in the XRD data, the annealing process is believed to have altered the morphology of the Au nanoinclusions, which resulted in the shift in hyperbolic regions seen here. This change in Au morphology also likely leads to a difference in the LSPR modes and difference in imaginary permittivity. The imaginary permittivity shows similar results to that of the As-Deposited with Thin Au Strip sample, being flat above 1000 nm. The As-Deposited with Thick Au Strip sample shows the highest difference from the other YIG–Au films by displaying Type-II hyperbolic properties. This is characterized by the real parallel (∥)

permittivity being negative and the perpendicular (⊥) permittivity being positive in most of the measured wavelength ranges (400–2000 nm). This suggests that Au has a more parallel distribution. Since this sample has the most Au composition among all samples, as shown in the XRD data in Fig. 1B, the Au may be thick enough to form a partially continuous Au layer within the YIG matrix. This potential Au microstructure would also result in a different LSPR mode than the other films due to the different shape. The imaginary permittivity for this sample shows the most notable difference from those of the previously measured samples due to the parallel direction having a negative permittivity (‖) from 400 nm to 1666 nm. A negative imaginary permittivity indicates plasmonic absorption, where light interacts with and is absorbed by the Au nanoinclusions. Beyond 1666 nm, the plasmonic absorption diminishes, and the film has increased transparency, behaving more like a dielectric material again, showing a preference for YIG after 1666 nm. The perpendicular (⊥) imaginary permittivity remains positive at all measured wavelengths, suggesting a dielectric nature in the out-of-plane direction and that the YIG matrix plays a larger role in the material's optical behavior in this direction.

Fig. 4C shows the transmittance data for all four films along with a blank GGG substrate. The blank substrate exhibits the highest transparency, as expected as it has no film, but among the films, the Annealed Pure YIG sample has the highest transparency. This serves as a baseline to see how adding in the plasmonic effects from the Au nanoinclusions affects the optical transparency of the following films. The Annealed with Thin Au Strip sample has the second highest transparency. Introducing Au into this film and the following films leads to a reduction in transparency, as seen from the absorption peak, indicating that plasmonic interactions occur within the film. This film shows an absorption peak at 590 nm, which is close to Au's absorption peak at 600 nm.[43] This is within the upper range for the LSPR peak for Au (500–600 nm), depending on the material's shape and size.[43] The higher absorption for the Annealed with Thin Au Strip sample than those of the other two YIG–Au samples could be attributed to changes in the morphology of the Au nanoinclusions and/or the annealing's contribution to fully developing the YIG garnet crystal structure and its optical transparency. The As-Deposited with Thin Au Strip sample has the third highest transparency and an absorption peak at 597 nm. This shift in the absorption peak position reflects a difference in the Au nanoinclusion morphology due to the lack of annealing which might have also left the YIG crystal structure not fully achieving the garnet crystal structure.[16] Finally, the film with the lowest transmittance is the As-Deposited with Thick Au Strip sample, which also has an absorption peak at 597 nm. The broader width of this peak could be due to this sample having more varied shapes and sizes of the Au nanoinclusions, increasing the absorption and scattering. This would suggest a higher distribution of LSPR modes for this film. The high concentration of Au in the sample also contributes to its low transmittance as the Au is not optically transparent like the YIG matrix. Instead, the amount of Au allows for stronger light scattering and absorption within the sample, as seen in this sample's imaginary permittivity data.

Overall, this shows that the optical properties including the optical anisotropy, hyperbolic properties, and transmittance can be tuned by adjusting the amount of Au put into the film during the deposition and annealing or without annealing. This Au morphology tuning allows for the variation of the hyperbolic properties, including switching between Type I and Type II hyperbolic properties and adjusting the hyperbolic ranges. To further show this, the As-Deposited Au Buffer sample on GGG substrate displays both Type I and Type II hyperbolic properties, as seen in SI Fig. S4, S5 and Table S2. This would allow for future applications to have adjustable responses to light, with some ranges now occurring in the visual spectrum as in the As-Deposited with Thick Au Strip sample, so that the YIG–Au nanocomposite thin films can be paired with other materials with a response in those wavelengths. This could allow these potential future devices to have more than one optical response under one optical trigger, allowing for greater efficiency.

Ferromagnetic resonance (FMR) was a vital measurement to perform on these samples considering the low Gilbert damping coefficient (α) of YIG. The FMR data for the four samples are presented in Fig. 5, and the corresponding magnetic hysteresis loops for all the samples can be found in SI Fig. S7. FMR would show if adding different amounts of Au, annealing, or leaving the films as-deposited would influence the α. Fig. 5A1–D1 show all the measured resonances for each of the samples. It is worth noting that the Annealed Pure YIG sample was measured over two days, resulting in a jump in peak height for some of the measured frequencies, and that the As-Deposited with Thin Au Strip sample did not have a resonance peak at 17 and 18 GHz unlike the other samples which were measured at 2–18 GHz, as outlined in the Experimental methods section. To aid in comparison, Fig. 5A2–D2 show a single resonance peak at 10 GHz for each sample. Fig. 5E and F show the frequencies, resonance peak widths, and the corresponding fields where the resonances occur, which are used to calculate α among other relevant parameters; these are reported together for convenience.

The Annealed Pure YIG sample shown in Fig. 5A1 and A2 has a low α at 9.66×10^{-4}, slightly higher than the values seen in the literature for this film grown *via* PLD, but still within the normal range for YIG films.[4,6] The minimal noise observed during the measurement shows a clean resonance behavior, probably due to annealing fully developing the garnet crystal structure.[16] It is worth noting the small secondary peak that occurs in the individually plotted resonance peak. These did not occur at every measured frequency, so 10 GHz was picked as the comparison frequency to highlight this as it is not visible on the combined frequency graph. This could point to inconsistencies in the film's microstructure that did not show up in the XRD data or the presence of defects that could cause a disruption of the spin wave's movement during the measurement through some two magnon scattering. The intrinsic reso-

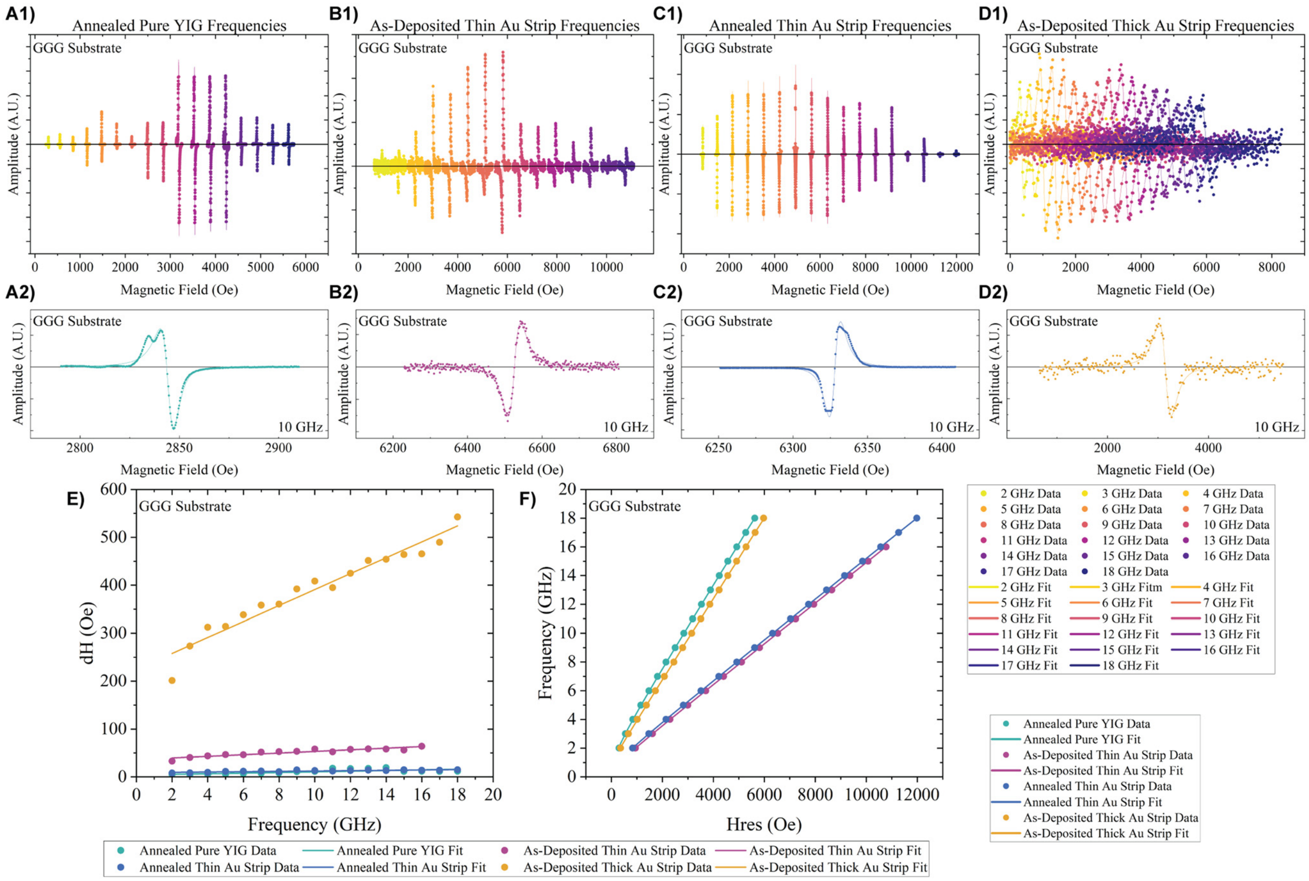

Fig. 5 Ferromagnetic resonance measurement results of (A) the Annealed Pure YIG sample, (B) As-Deposited with Thin Au Strip sample, (C) Annealed with Thin Au Strip sample, and (D) As-Deposited with Thick Au Strip sample. (1) All measured frequencies. (2) Selected 10 GHz frequency. (E) Graph showing the width of the frequency peaks *versus* the frequency they appear at for all four shown samples. (F) Graph showing the frequency resonance peaks appear at *versus* where the peaks occur for all four shown samples.

nance frequency is primarily determined by YIG's internal magnetic fields, showing the importance of the Pure YIG sample as a comparison.

Next, Fig. 5B1 and B2 show the As-Deposited with Thin Au Strip sample with a higher α at 1.19×10^{-3}, suggesting that the spin waves do not propagate as efficiently in this film, due to the Au phase introducing some two-magnon scattering. The noise seen in the measurement, especially prominent near the baseline in the single peak plot, shows that the film is more non-uniform. This could be due to both the non-annealed YIG crystal structure and the morphology of the Au nanoinclusions being more disordered. Additionally, the resonances for this sample occur at much higher fields than those of the Annealed Pure YIG sample, which can also be seen in Fig. 5F, indicating that the Au nanoinclusions have introduced magnetic anisotropy into this film, likely due to localized interfacial strain between the YIG and Au phases. This change in anisotropy results in the change in α as it affects the spin wave propagation, although this change in anisotropy is generally understood to be small. The distribution of the Au nanoinclusions allows for this to occur regularly throughout the film, without the nanoinclusions blocking the spin wave propagation. Despite the higher α than those of many of the annealed samples, this sample has the lowest Gilbert damping coefficient among all the as-deposited films, including the ones presented in the SI. This is seen in SI Table S3 and Fig. S10, which list out all samples deposited on GGG substrates, showing their Gilbert damping coefficient along with other parameters from the FMR fit and a graph representing the Gilbert damping coefficient *versus* relative amount of Au in the films. This could have also occurred due to the improved YIG growth seen in Fig. 1, supported by only this Thin Au Strip sample showing an improved magnetic damping out of the three samples deposited with Au.

The FMR data of the Annealed with Thin Au Strip sample are shown in Fig. 5C1 and C2 with the lowest measured α at 2.84×10^{-4}, indicating the best spin wave transmission, abnormal due to Au not normally enhancing YIG's internal magnetic fields. The low noise seen again in this sample helps achieve this with the more uniform film, as also seen in the Annealed Pure YIG sample. Annealing would have changed the Au morphology within the film, making it more consistent than the as-deposited film, as demonstrated by the XRD data showing a stronger Au (220) peak and other weaker Au peaks when compared to those of the substrate. Also as stated previously, annealing is believed to help with the YIG crystallinity which is one of the most important factors for the Gilbert damping coefficient.[16] The resonance fields are also at higher levels than those of the Annealed Pure YIG sample, supporting that the Au nanoinclusions introduced magnetic anisotropy which helped lower the α, but the Thin Au Strip deposition might also have helped by increasing the YIG film quality, as seen from the XRD data. This also could have occurred due to increased strain in the film, supporting increased YIG film quality, and boundary condition changes. The introduction of the VAN microstructure allows for more of these boundaries and local YIG–Au strain interfaces that other microstructures would not, causing a greater shift than expected. The moderate amount of strain introduced enabled energy dissipation during the resonance, leading to another contribution of the lower magnetic damping coefficient. This increase in vertical phase boundaries and strain coupling could contribute to the overall improved damping properties in the As-Deposited with Thin Au Strip sample.

Finally, the As-Deposited with Thick Au Strip sample has its α at 2.33×10^{-2}. This sample has the highest α, the widest resonance peaks, and the most measured noise of any of the samples shown here. The high α shows that there is too much Au in the YIG–Au system and the benefits of Au in improving the FMR are reduced, but FMR can still be performed on this film. The extra Au in this film prevents the spin wave from transmitting as easily throughout the film, but instead spin scattering starts occurring within the film due to the Au nanoinclusions. There is also a decrease in the magnetic anisotropy, as demonstrated in the fields that the resonances occur at decreasing again, almost back to where the Annealed Pure YIG Sample's resonances occur, around 3000 Oe for the 10 GHz frequency. The wide resonance peaks, also shown in Fig. 5E, also demonstrate how the more disordered Au nanoinclusions increase the spin scattering through two-magnon scattering due to the large amount of defects they introduce into the film. The large increase in measurement noise again shows the disorder within the film, which is possible both due to the Au and the non-annealed YIG crystal structure. This demonstrates how at lower Au contents, strain coupling between YIG and Au dominates allowing for a lower α, while at higher Au contents, the large amounts of Au nanoinclusions cause significant scattering, causing an increase in α. A list of all Gilbert damping coefficients can be seen in Table 1. Further work can focus on the optimal ratios of YIG to Au to determine if a better damping property can be achieved.

Table 1 List of samples and their Gilbert damping coefficients

Sample name	Gilbert damping coefficient (α)
Annealed Pure YIG	9.66×10^{-4}
As-Deposited with Thin Au Strip	1.19×10^{-3}
Annealed with Thin Au Strip	2.84×10^{-4}
As-Deposited with Thick Au Strip	2.33×10^{-2}

Overall, the FMR data show that the addition of Au can first reduce and then increase the Gilbert damping coefficient (α) as the Au composition increases. It is possible to get a lower α and optimized spin wave transmission than the Annealed Pure YIG sample through the addition of the Au nanoinclusions, but annealing is still necessary. The addition of Au can introduce magnetic anisotropy into the film. However, adding too much Au, as seen in the As-Deposited with Thick Au Strip sample, can lead to increased spin scattering and a higher damping, with α closer to those observed for materials such as NiFe instead of YIG, due to the large number of defects now introduced into the film.[1] The sample can still measure FMR with a damping coefficient for the films and could be used for some spintronic applications. Room temperature magneto-optical Kerr effect (MOKE) measurements were also performed on the As-Deposited Thin Au Strip and the Annealed Thin Au Strip samples, and can be seen in SI Fig. S12, to further understand how the optical and magnetic properties were linked. The Annealed sample, while having a weaker saturation, has less noise in both the P-MOKE and L-MOKE measurements, again showing the importance of annealing for YIG. The higher saturation that the As-Deposited Thin Au Strip Sample achieves could be due to the higher magnetic anisotropy caused by the Au nanoinclusions.

While there are prior studies on YIG–Au multilayer designs, this is the first demonstration of a YIG–Au VAN on a GGG substrate and is also the first demonstration of a YIG–Au PiM nanocomposite on a STO substrate.[24,25] The property measurements for the STO substrate samples are summarized in SI Fig. S15–S20. While previous work has shown the effects of adding Au layers on the optical properties and magnetic properties of YIG, some important factors have been overlooked, specifically the Gilbert damping coefficient (α). This work has shown that certain amounts of Au incorporation can help tune the magnetic anisotropy to achieve a lower α than that of a pure YIG film, for both the annealed and as-deposited conditions. An additional explanation for this effect is that the thin Au strip helps the YIG film grow in a more crystalline order when compared with the Pure YIG film. In addition, the small amount of Au incorporation also facilitates the nucleation and growth of epitaxial YIG on GGG which results in better epitaxy quality and enhanced FMR properties as evidenced in Fig. 5. The addition of Au to the system allows for the tunability of both the magnetic and optical properties. However, this work has shown that there can be a trade-off between the two properties. If a Type II, or metallic, hyperbolic system is desired, this work has shown that the magnetic properties could be worse. Conversely, an improved Gilbert damping coefficient only resulted in Type I hyperbolic properties. This does show that the YIG–Au system can be designed for specific applications. A sample set, named Au Buffer, has its data shown in the SI, and it shows an interesting trend. Both Type I and Type II hyperbolic properties are shown by the As-Deposited film, as seen in SI Fig. S4 and S5, and the ranges are presented in SI Table S2. These buffer layer samples have a higher magnetic damping property than Pure

YIG in both the Annealed and As-Deposited states, likely due to the small amount of Au not allowing for strain coupling leading to increased anisotropy, and instead only acting as defects for two-magnon scattering. However, the As-Deposited with Au Buffer film shows an opportunity for further property tuning by representing both hyperbolic properties due to the small Au nanoparticles at the substrate–film interface, but does continue to show the trade-offs that the introduction of Au can have on the system.

Future work based on this study could focus on incorporating different plasmonic metals such as silver (Ag) and copper (Cu) in YIG VANs, both of which have been demonstrated in YIG-multilayer systems previously.[26–28] This would allow for different plasmonic resonances to be integrated in YIG thin films for wavelength-selective opto-spintronic devices. More studies into the effects of co-deposition of plasmonic metals, and particularly more with Au, could parse out if the improved magnetic damping only occurs due to the improved growth or if the Au helps introduce magnetic anisotropy outside of this, and if this effect could be repeated with the other plasmonic metals. Further work on exploring YIG–Au ratios can be attempted to determine if an optimal ratio can be achieved for lowering the Gilbert damping coefficient. This work only looked at two Au concentrations, and found that there is a point of too much Au within the film. Further study can also explore the size and distribution of the Au nanoinclusions on the GGG substrates to achieve smaller and regularly spaced nanoinclusions for a lower Gilbert damping coefficient.

Other directions could include implementing a magnetic secondary phase in YIG. This would introduce new magnetic coupling between YIG and the secondary phase, such as different magnon transport mechanisms with different Gilbert damping coefficients. These novel YIG-based VAN systems also call for future developments such as growth integration on device relevant substrates, *e.g.*, Si, with optimized epitaxial growth quality, which could enable unique applications in future spintronic and opto-spintronic devices. This would utilize both the low magnetic damping and light–matter interactions seen in this work to be used for future devices where spin waves and photons are coupled in the nanoscale microstructure design.

Conclusion

This work explored multiple YIG–Au nanocomposite thin films, with YIG as the matrix and Au as nanoinclusions. The effects of Au content and film annealing on the overall nanostructure, optical properties, and ferromagnetic resonance responses were examined. The addition of Au introduced optical anisotropy and hyperbolic properties into the nanocomposites, an effect absent in the Pure YIG film. Optical anisotropy and Type-I and Type-II hyperbolic responses were observed under different Au compositions and deposition conditions. Au incorporation also affected the magnetic damping properties, with the Annealed with Thin Au Strip sample having a lower Gilbert damping coefficient (α) than the Annealed Pure YIG sample (*i.e.*, 2.84×10^{-4} *vs.* 9.66×10^{-4}) despite identical deposition conditions. The Thin Au Strip samples showed improved YIG film growth in the XRD results, so the improved magnetic damping could have resulted from this effect. This reduction from improved growth from co-deposition still occurs despite the Au defects within the YIG matrix resulting in two-magnon scattering. However, the As-Deposited with Thick Au Strip sample, which had Type-II hyperbolic properties at all measured wavelengths, had the highest α (2.33×10^{-2}) among all measured samples, more similar to other materials such as NiFe, due to the increased Au content causing a high amount of two-magnon scattering from the introduction of the Au defects within the YIG film, but not exactly the same value. These findings demonstrate that both magnetic and optical properties can be tuned by tailoring Au concentration and with or without the annealing process. This shows great potential of YIG–Au based nanocomposites for future multifunctional device applications, such as high efficiency spin-wave guides and opto-spintronic devices where light can be used to control the spin dynamics.

Experimental methods

The YIG ($Y_3Fe_5O_{12}$) target was prepared using iron yttrium oxide powder from Thermo Fisher. The powder was pressed into a 2 inch (50.8 mm) diameter target and sintered at 1200 °C for 10 hours. There were two Au strips used for depositions described as the Thin Au Strip with a width of 2.6 mm and the Thick Au Strip with a width of 5.7 mm. The deposition conditions were optimized for the Pure YIG growth, then kept consistent for all depositions, and are as follows. These were done through pulsed laser deposition (PLD) with a KrF excimer laser (Lambda Physik, λ = 248 nm). A laser energy of 400 mJ, an atmosphere of 50 mTorr O_2, a temperature of 850 °C, a 4.5 cm distance between the target and substrate(s), a frequency rate of 5 Hz, and a pulse number of 5000 were used for all depositions. For the depositions with the Thin and Thick Au strip, the strip was pasted onto the target using a small amount of silver paste to keep it in place during the deposition. The target was then rotated at a speed of 30° per second so that the deposition would alternate between YIG and Au, with overall more YIG being deposited. The laser track occurred at roughly 80% away from the center of the target. For the Pure YIG deposition, the target was both rotated and rastered so that the entire surface was used.

For the depositions with a YIG–Au buffer layer, with their data only shown in the SI, the YIG-Au buffer layer was first deposited with a frequency of 5 Hz and 100 pulses, with all other deposition conditions kept consistent (laser energy of 400 mJ, 50 mTorr O_2 pressure, temperature of 850 °C, and 4.5 cm target to substrate(s) distance). The Au strip used was the Thick Au strip, and it was pasted in the same manner as the Thick Au deposition. A second pure YIG target was used after the YIG–Au buffer layer deposition to deposit a layer of only

YIG, with the same deposition conditions as those of the Pure YIG sample (5 Hz, 5000 pulses, laser energy of 400 mJ, 50 mTorr O_2 particle pressure, temperature of 850 °C, and 4.5 cm target to substrate(s) distance).

The annealed films were held at 850 °C for one hour post-deposition under 50 mTorr O_2 before cooling to room temperature at 15 °C min^{-1} under the O_2 atmosphere. The As-Deposited samples were cooled at 15 °C min^{-1} and under 50 mTorr O_2 directly after deposition. A list of all the depositions conducted can be found in SI Table S1.

Characterization to confirm the crystallinity, elemental, and microstructural qualities of the thin film samples was performed with an PANalytical Empyrean XRD with a Cu Kα radiation source and a high-resolution Thermo Fisher Scientific TALOS 200× with TEM and STEM operated at 200 kV. The STEM has EDS capability through a FEI Titan™ G2 80–200 STEM with a Cs probe corrector and ChemiSTEM™ technology (X-FEG™ and SuperX™ energy-dispersive X-ray spectroscopy (EDS) with four windowless silicon drift detectors) also operated at 200 kV. Sample preparation for the samples grown on STO substrates was performed by hand by thinning the sample through manual grinding and polishing. A thin area was made in the sample through dimpling and more polishing, and the sample was then finished with a PIPS II Model 695 ion miller from Gatan. Sample preparation for the samples grown on GGG substrates was performed with a FIB cut and lift-out using an FEI Helios G4 dual beam SEM. Before the FIB cut could be performed, a Pt layer had to be deposited on the films due to YIG's insulating nature.

Magnetic hysteresis measurements were completed with an MPMS Model 3 (Quantum Design) with an EverCool SQUID magnetometer in the user facility of the Birck Nanotechnology Center at Purdue University (see birck.research.purdue.edu). The magnetic moment *versus* applied field measurement was completed in both the in-plane and out-of-plane directions at both 300 K and 10 K up to a field of ±20 kOe.

The ferromagnetic resonance measurements were performed with a PPMS DynaCool (Quantum Design) and a CryoFMR add-on (NanOsc) in the user facility of the Birck Nanotechnology Center at Purdue University (see birck.research.purdue.edu). The frequency range of the microwave source used was 2–18 GHz, measured in 1 GHz increments. The sample was placed on a coplanar waveguide in the in-plane direction, or with the applied magnetic field along the length of the film, and the measurement was performed at 300 K. The instrument measured the variation of the absorbed power as a function of the magnetic field (dP/dH) at the mentioned frequencies. The resonance field (H_{res}) and peak-to-peak linewidth (ΔH) of the FMR graphs were measured at each frequency and for each peak that occurred with the NanOsc program. The program was then able to calculate other reported parameters such as the Gilbert damping coefficient (α) and the gyromagnetic ratio (γ) based on the standard FMR fitting equations.

MOKE measurements were performed using a home-built system with a photoelastic modulator (PEM), a GMW dipole magnet and a He–Ne laser of wavelength 632.8 nm in both polar and longitudinal configurations at room temperature. For the longitudinal configuration, the laser was incident at an angle of approximately 25°.

Spectroscopic ellipsometry measurements were performed on a J.A. Woollam RC2 ellipsometer to determine the dielectric permittivity of the thin films. The parameters psi (Ψ) and delta (Δ) were collected at 55°, 65°, and 75° from 400 to 2000 nm. Different fits (uniaxial/isotropic) were applied depending on whether the film was pure YIG or a YIG–Au composite. Transmittance measurements were performed after all other measurements were completed, as the backside of the substrate needed to be manually polished for the measurement to improve optical clarity. A PerkinElmer LAMBDA 1050 UV/VIS spectrophotometer was used for normal incident depolarized transmittance measurement of the thin films.

Author contributions

Lizabeth Quigley – Conceptualization, lead; investigation, lead; methodology, lead; investigation, lead; project administration, lead; validation, lead; visualization, lead; and writing – original draft, lead. Katrina Evancho – Investigation, supporting. Claire A. Mihalko – Investigation, supporting. Yizhi Zhang – Investigation, supporting. Chang Liu – Investigation, supporting. Max Chhabra – Investigation, supporting. Bharat Giri – Investigation, supporting. Jialong Huang – Investigation, supporting. Abhijeet Choudhury – Investigation, supporting. Jeremy Gan – Investigation, supporting. Zhengliang Lin – Investigation, supporting. Xiaoshan Xu – Resources, supporting. Ping Lu – Investigation, supporting. Raktim Sarma – Supervision, supporting. Aleem Siddiqui – Supervision, supporting. Haiyan Wang – Funding acquisition, lead; resources, lead; supervision, lead; and writing – review & editing, supporting.

Conflicts of interest

There are no conflicts to declare.

Data availability

The data supporting this article have been included as part of the supplementary information (SI). Supplementary information is available. This includes a closer view near zero for the optical data see in the paper, all of the data for samples deposited on GGG substrates, and all of the data for samples deposited on STO substrates. See DOI: https://doi.org/10.1039/d5nr03907j.

Acknowledgements

This work was supported by the U.S. Department of Energy, Office of Science, Basic Energy Sciences under Award

DE-SC0020077. This work was also partially supported by the Laboratory Directed Research and Development program at Sandia National Laboratories, and performed, in part, at the Center for Integrated Nanotechnologies, an Office of Science User Facility operated for the U.S. Department of Energy (DOE) Office of Science by Los Alamos National Laboratories and Sandia National Laboratories. Sandia National Laboratories is a multiprogram laboratory managed and operated by National Technology and Engineering Solutions of Sandia, LLC, a wholly owned subsidiary of Honeywell International, Inc., for the U.S. Department of Energy's National Nuclear Security Administration under contract DE-NA0003525. This paper describes objective technical results and analysis. Any subjective views or opinions that might be expressed in the paper do not necessarily represent the views of the U.S. Department of Energy or the United States Government. Additionally, this work was supported by the Sandia National Laboratories Diversity Initiative Fellowship (L.Q.). The high-resolution STEM work was partially supported by the U.S. National Science Foundation DMR-2016453. L.Q. is also thankful for the support from the Purdue University Doctoral Graduate Fellowship for the first two years of her Ph.D. study.

References

1 L. Caretta and C. O. Avci, Domain Walls Speed up in Insulating Ferrimagnetic Garnets, *APL Mater.*, 2024, **12**(1), 011106, DOI: 10.1063/5.0159669.

2 A. A. Serga, A. V. Chumak and B. Hillebrands, YIG Magnonics, *J. Phys. D: Appl. Phys.*, 2010, **43**(26), 264002, DOI: 10.1088/0022-3727/43/26/264002.

3 A. Z. Arsad, A. W. M. Zuhdi, N. B. Ibrahim and M. A. Hannan, Recent Advances in Yttrium Iron Garnet Films: Methodologies, Characterization, Properties, Applications, and Bibliometric Analysis for Future Research Directions, *Appl. Sci.*, 2023, **13**(2), 1218, DOI: 10.3390/app13021218.

4 R. Kumar, B. Samantaray, S. Das, K. Lal, D. Samal and Z. Hossain, Damping in Yttrium Iron Garnet Films with Interface, *Phys. Rev. B*, 2022, **106**(5), 054405, DOI: 10.1103/PhysRevB.106.054405.

5 C. Hauser, T. Richter, N. Homonnay, C. Eisenschmidt, M. Qaid, H. Deniz, D. Hesse, M. Sawicki, S. G. Ebbinghaus and G. Schmidt, Yttrium Iron Garnet Thin Films with Very Low Damping Obtained by Recrystallization of Amorphous Material, *Sci. Rep.*, 2016, **6**(1), 20827, DOI: 10.1038/srep20827.

6 M. C. Onbasli, A. Kehlberger, D. H. Kim, G. Jakob, M. Kläui, A. V. Chumak, B. Hillebrands and C. A. Ross, Pulsed Laser Deposition of Epitaxial Yttrium Iron Garnet Films with Low Gilbert Damping and Bulk-like Magnetization, *APL Mater.*, 2014, **2**(10), 106102, DOI: 10.1063/1.4896936.

7 T. Liu, H. Chang, V. Vlaminck, Y. Sun, M. Kabatek, A. Hoffmann, L. Deng and M. Wu, Ferromagnetic Resonance of Sputtered Yttrium Iron Garnet Nanometer Films, *J. Appl. Phys.*, 2014, **115**(17), 17A501, DOI: 10.1063/1.4852135.

8 A. Rashedi, M. Ebrahimi, Y. Huang, M. J. Rudd and J. P. Davis, YIG Photonic Crystals, *arXiv*, 2024. DOI: 10.48550/arXiv.2412.05361.

9 Y. S. Dadoenkova, N. N. Dadoenkova, I. L. Lyubchanskii, J. W. Kłos and M. Krawczyk, Confined States in Photonic-Magnonic Crystals with Complex Unit Cell, *J. Appl. Phys.*, 2016, **120**(7), 073903, DOI: 10.1063/1.4961326.

10 L. J. A. van Tilburg, F. J. Buijnsters, A. Fasolino, T. Rasing and M. I. Katsnelson, Nonlinear Effects in the Propagation of Optically Generated Magnetostatic Volume Mode Spin Waves, *Phys. Rev. B*, 2017, **96**(5), 054437, DOI: 10.1103/PhysRevB.96.054437.

11 J. F. K. Cooper, C. J. Kinane, S. Langridge, M. Ali, B. J. Hickey, T. Niizeki, K. Uchida, E. Saitoh, H. Ambaye and A. Glavic, Unexpected Structural and Magnetic Depth Dependence of YIG Thin Films, *Phys. Rev. B*, 2017, **96**(10), 104404, DOI: 10.1103/PhysRevB.96.104404.

12 R. Peña-Garcia, A. Delgado, Y. Guerra and E. Padrón-Hernández, Yig Films With Low Magnetic Damping Obtained By Solgel On Silicon (100), *Mater. Lett.*, 2015, **161**, 384–386, DOI: 10.1016/j.matlet.2015.08.147.

13 B. Bhoi, Bulk-like Magnetization and Improved Microwave Properties of Polycrystalline YIG ($Y_3Fe_5O_{12}$) Films Grown on Quartz Substrates by Pulsed Laser Deposition, *J. Alloys Compd.*, 2019, **797**, 523–528, DOI: 10.1016/j.jallcom.2019.05.108.

14 N. A. Shepelin, Z. P. Tehrani, N. Ohannessian, C. W. Schneider, D. Pergolesi and T. Lippert, A Practical Guide to Pulsed Laser Deposition, *Chem. Soc. Rev.*, 2023, **52**(7), 2294–2321, DOI: 10.1039/D2CS00938B.

15 B. Bhoi, B. Kim, Y. Kim, M.-K. Kim, J.-H. Lee and S.-K. Kim, Stress-Induced Magnetic Properties of PLD-Grown High-Quality Ultrathin YIG Films, *J. Appl. Phys.*, 2018, **123**(20), 203902, DOI: 10.1063/1.5031198.

16 R. Kumar, Z. Hossain and R. C. Budhani, Effects of Post-Deposition Annealing on the Structure and Magnetization of PLD Grown Yttrium Iron Garnet Films, *J. Appl. Phys.*, 2017, **121**(11), 113901, DOI: 10.1063/1.4978310.

17 H. B. Vasili, B. Casals, R. Cichelero, F. Macià, J. Geshev, P. Gargiani, M. Valvidares, J. Herrero-Martin, E. Pellegrin, J. Fontcuberta and G. Herranz, Direct observation of multivalent states and 4f→3d charge transfer in Ce-doped yttrium iron garnet thin films, *Phys. Rev. B*, 2017, **96**(1), 014433, DOI: 10.1103/PhysRevB.96.014433.

18 M. Kuila, U. Deshpande, R. J. Choudhary, P. Rajput, D. M. Phase and V. Raghavendra Reddy, Study of Magneto-Optical Activity in Cerium Substituted Yttrium Iron Garnet (Ce:YIG) Epitaxial Thin Films, *J. Appl. Phys.*, 2021, **129**(9), 093903, DOI: 10.1063/5.0039647.

19 B. A. Şentürk and Y. Öztürk, Magnetic Properties of Sol-Gel Produced Cerium Substituted YIG Thin Film, in 2024 *IEEE 14th International Conference Nanomaterials: Applications & Properties (NAP)*, 2024, pp. 1–4. DOI: 10.1109/NAP62956.2024.10739739.

20 R. Kumar, B. Samantaray and Z. Hossain, Ferromagnetic Resonance Studies of Strain Tuned Bi:YIG Films, *J. Phys.: Condens. Matter*, 2019, **31**(43), 435802, DOI: 10.1088/1361-648X/ab2e93.

21 P. Sellappan, C. Tang, J. Shi and J. E. Garay, An Integrated Approach to Doped Thin Films with Strain-Tunable Magnetic Anisotropy: Powder Synthesis, Target Preparation and Pulsed Laser Deposition of Bi:YIG, *Mater. Res. Lett.*, 2017, **5**(1), 41–47, DOI: 10.1080/21663831.2016.1195779.

22 Y. Jia, Z. Liang, H. Pan, Q. Wang, Q. Lv, Y. Yan, F. Jin, D. Hou, L. Wang and W. Wu, Bismuth Doping Enhanced Tunability of Strain-Controlled Magnetic Anisotropy in Epitaxial Y3Fe5O12(111) Films, *Chin. Phys. B*, 2023, **32**(2), 027501, DOI: 10.1088/1674-1056/ac67cc.

23 J. Lu, D. Zhang, R. L. Paldi, Z. He, P. Lu, J. Deitz, A. Ahmad, H. Dou, X. Wang, J. Liu, Z. Hu, B. Yang, X. Zhang, A. A. El-Azab and H. Wang, Abnormal In-Plane Epitaxy and Formation Mechanism of Vertically Aligned Au Nanopillars in Self-Assembled CeO_2–Au Metamaterial Systems, *Mater. Horiz.*, 2023, **10**(8), 3101–3113, DOI: 10.1039/D3MH00233K.

24 Z. Li, X. Zhang, D. Zhang, B. Lie, H. Meng, J. Xu, Z. Zhong, X. Tang, H. Zhang and L. Jin, Magnetization Dynamics in the YIG/Au/YIG Magnon Valve, *APL Mater.*, 2022, **10**(2), 021101, DOI: 10.1063/5.0081104.

25 M. Akyol, N. Demiryurek, O. Iloglu, K. U. Tumen, F. Karadag and A. Ekicibil, Structural, Magnetic and Optical Properties of Au/YIG, YIG/Au and Au/YIG/Au Multilayer Thin Film Stacks, *J. Magn. Magn. Mater.*, 2020, **493**, 165704, DOI: 10.1016/j.jmmm.2019.165704.

26 J. G. S. Santos, E. F. Silva, W. O. Rosa, F. Bohn and M. A. Correa, Role of the Spin-Orbit Coupling on the Effective Damping Parameter in Y3Fe5O12/(Ag,W) Bilayers Explored through Magnetoimpedance Effect, *Mater. Lett.*, 2019, **256**, 126662, DOI: 10.1016/j.matlet.2019.126662.

27 H. L. Wang, C. H. Du, Y. Pu, R. Adur, P. C. Hammel and F. Y. Yang, Scaling of Spin Hall Angle in 3d, 4d, and 5d Metals from Y3Fe5O2Metal Spin Pumping, *Phys. Rev. Lett.*, 2014, **112**(19), 197201, DOI: 10.1103/PhysRevLett.112.197201.

28 C.-K. Hu, J.-X. Lin, H.-A. Liu, W.-H. C. Chien, W.-B. Wu, J.-S. Lee, C.-R. Lin, S. Mangin, J. Chen and H.-S. Hsu, Manipulation of Energy-Resolved Magneto–Optical Effect in Yttrium Iron Garnet Films Achieved by Covering with Nonmagnetic Metals, *Chin. J. Phys.*, 2024, **90**, 717–725, DOI: 10.1016/j.cjph.2024.04.027.

29 R. L. Paldi, X. Sun, X. Wang, X. Zhang and H. Wang, Strain-Driven In-Plane Ordering in Vertically Aligned ZnO–Au Nanocomposites with Highly Correlated Metamaterial Properties, *ACS Omega*, 2020, **5**(5), 2234–2241, DOI: 10.1021/acsomega.9b03356.

30 N. A. Bhatt, R. L. Paldi, J. P. Barnard, J. Lu, Z. He, B. Yang, C. Shen, J. Song, R. Sarma, A. Siddiqui and H. Wang, ZnO-Au Hybrid Metamaterial Thin Films with Tunable Optical Properties, *Crystals*, 2024, **14**(1), 65, DOI: 10.3390/cryst14010065.

31 J. Huang, T. Jin, S. Misra, W. Han, Z. Qi, Y. Dai, X. Sun, L. Li, J. Okkema, H.-T. Chen, P.-T. Lin, X. Zhang and H. Wang, Tailorable Optical Response of Au–LiNbO3 Hybrid Metamaterial Thin Films for Optical Waveguide Applications, *Adv. Opt. Mater.*, 2018, **6**(19), 1800510, DOI: 10.1002/adom.201800510.

32 J. Huang, L. Li, P. Lu, Z. Qi, X. Sun, X. Zhang and H. Wang, Self-Assembled Co–BaZrO3 Nanocomposite Thin Films with Ultra-Fine Vertically Aligned Co Nanopillars, *Nanoscale*, 2017, **9**(23), 7970–7976, DOI: 10.1039/C7NR01122A.

33 B. Zhang, J. Huang, J. Jian, B. X. Rutherford, L. Li, S. Misra, X. Sun and H. Wang, Tuning Magnetic Anisotropy in Co–BaZrO3 Vertically Aligned Nanocomposites for Memory Device Integration, *Nanoscale Adv.*, 2019, **1**(11), 4450–4458, DOI: 10.1039/C9NA00438F.

34 J. Liu, X. Wang, X. Gao, H. Wang, B. Zhang, D. Zhang, M. Kalaswad, J. Huang and H. Wang, Integration of Self-Assembled BaZrO3-Co Vertically Aligned Nanocomposites on Mica Substrates toward Flexible Spintronics, *Cryst. Growth Des.*, 2022, **22**(1), 718–725, DOI: 10.1021/acs.cgd.1c01227.

35 Z. Hu, J. Lu, H. Dou, J. Shen, J. P. Barnard, J. Liu, X. Zhang and H. Wang, Template-Assisted Growth of Co-BaTiO3 Vertically Aligned Nanocomposite Thin Films with Strong Magneto-Optical Coupling Effect, *Nano Res.*, 2024, **17**(4), 3130–3138, DOI: 10.1007/s12274-023-6054-7.

36 J. Huang, X. Wang, X. L. Phuah, P. Lu, Z. Qi and H. Wang, Plasmonic Cu Nanostructures in ZnO as Hyperbolic Metamaterial Thin Films, *Mater. Today Nano*, 2019, **8**, 100052, DOI: 10.1016/j.mtnano.2019.100052.

37 N. A. Bhatt, L. Quigley, S. Zhou, A. Gnanasabai, A. Choudhury, Y. Zhang, J. Shen, J. Lu, A. Siddiqui, R. Sarma and H. Wang, Morphology and Property Tuning in ZnO–Ni Hybrid Metamaterials in Vertically Aligned Nanocomposite (VAN) Form, *Nanoscale Adv.*, 2025, **7**(11), 3528–3538, DOI: 10.1039/D5NA00207A.

38 Z. He, J. Jian, L. Quigley, N. A. Bhatt, J. P. Barnard, C. A. Mihalko, H. Wang, X. L. Phuah, J. Lu, X. Xu and H. Wang, Magnetic Ni-Nanoinclusions in VO2 Thin Films for Broad Tuning of Phase Transition Properties, *Adv. Phys. Res.*, 2023, **2**(12), 2300031, DOI: 10.1002/apxr.202300031.

39 B. Zhang, J. Huang, B. X. Rutherford, P. Lu, S. Misra, M. Kalaswad, Z. He, X. Gao, X. Sun, L. Li and H. Wang, Tunable, Room-Temperature Multiferroic Fe-BaTiO3 Vertically Aligned Nanocomposites with Perpendicular Magnetic Anisotropy, *Mater. Today Nano*, 2020, **11**, 100083, DOI: 10.1016/j.mtnano.2020.100083.

40 M. Kalaswad, B. Zhang, X. Wang, H. Wang, X. Gao and H. Wang, Integration of Highly Anisotropic Multiferroic BaTiO3–Fe Nanocomposite Thin Films on Si towards Device Applications, *Nanoscale Adv.*, 2020, **2**(9), 4172–4178, DOI: 10.1039/D0NA00405G.

41 J. Liu, X. Wang, H. Wang, Z. Qi, J. P. Barnard, B. Zhang and H. Wang, Multiferroic Self-Assembled BaTiO3–Fe Vertically Aligned Nanocomposites on Mica Substrates toward

Flexible Electronics, *ACS Appl. Electron. Mater.*, 2022, **4**(8), 4077–4084, DOI: 10.1021/acsaelm.2c00712.

42 L. Quigley, J. Lu, C. A. Mihalko, J. Huang, J. Gan, K. Evancho, M. Chhabra, R. Sarma, A. Siddiqui, P. Lu and H. Wang, Strong Structural and Property Anisotropy in CeO_2-NiFe Hybrid Metamaterials Toward Self-Assembled Magnon Nanostructures, *Small Sci.*, 2500070. DOI: 10.1002/smsc.202500070.

43 M. A. Alebrahim, A. A. Ahmad, A. B. Migdadi and Q. M. Al-Bataineh, Localize Surface Plasmon Resonance of Gold Nanoparticles and Their Effect on the Polyethylene Oxide Nanocomposite Films, *Phys. B*, 2024, **679**, 415805, DOI: 10.1016/j.physb.2024.415805.

44 R. L. Paldi, Z. Qi, S. Misra, J. Lu, X. Sun, X. L. Phuah, M. Kalaswad, J. Bischoff, D. W. Branch, A. Siddiqui and H. Wang, Nanocomposite-Seeded Epitaxial Growth of Single-Domain Lithium Niobate Thin Films for Surface Acoustic Wave Devices, *Adv. Photonics Res.*, 2021, **2**(6), 2000149, DOI: 10.1002/adpr.202000149.